Population Mixing in Asymmetric Magnetic Reconnection with a Guide Field

M. Hesse, L. J. Chen, Y.-H. Liu, N. Bessho, and J. L. Burch

Phys. Rev. Lett. **118**, 145101 — Published 3 April 2017

DOI: 10.1103/PhysRevLett.118.145101

Population Mixing in Asymmetric Magnetic Reconnection with a Guide Field

M. Hesse[1,3], L. J. Chen[1], Y. -H. Liu[1], N. Bessho[1], and J. L. Burch[2]

[1] Heliophysics Science Division, NASA Goddard Space Flight Center, Greenbelt, Maryland, USA
[2] Southwest Research Institute, San Antonio TX, USA
[3] now at: Birkeland Centre for Space Science, Dept. of Physics and Technology, University of Bergen, Bergen, Norway

ABSTRACT

We investigate how population mixing leads to structured electron distribution functions in asymmetric guide-field magnetic reconnection based on particle-in-cell simulations. The change of magnetic connectivity patches populations from different inflow regions to form multi-component distributions in the exhaust, illustrating the direct consequence of the breaking and rejoining of magnetic flux tubes. Finite Larmor radius (FLR) effects of electrons accelerated by the perpendicular electric fields result in crescent-type nongyrotropic distributions. A new type of nongyrotropy is found to be caused by the combined effects of FLR and velocity dispersion of electrons accelerated by the parallel electric field. The patching together of populations, and the effects of acceleration and FLR form the first steps of mixing in the exhaust and separatrix regions.

I. INTRODUCTION

Magnetic reconnection is a key process in collisionless plasmas, in the laboratory [1], the solar atmosphere [2], the interplanetary space [3], and the space environments of magnetized planets [4,5]. Energy, mass, momentum, and magnetic flux transport into Earth's magnetic cavity is facilitated by reconnection at the magnetopause. Reconnection here connects plasmas from the hot, tenuous plasma from the magnetosphere with the cold, dense plasma from the magnetosheath. Magnetopause reconnection is therefore typically asymmetric in upstream conditions – which is generic for many applications elsewhere.

For this reason magnetopause reconnection has attracted considerable attention [e.g., 5-8]. Recently, the Magnetospheric Multiscale (MMS) mission [e.g., 9-10] provided unprecedented high-resolution electron-scale measurements regarding magnetopause reconnection [11,26]. Consequently, asymmetric reconnection has seen multiple new fronts in observations and modeling [e.g., 11-27], including discoveries of the electron diffusion region at the magnetopause in both planar geometries [11,26] as well as in configurations with guide magnetic fields [23]. Magnetopause reconnection typically involves significant guide fields, yet most simulations addressing the kinetic structures of the diffusion region are for negligible guide fields.

Theory and modeling research has shown that reconnection can generate multi-component nongyrotropic electron distribution functions inside the electron diffusion region [24-27]. These features were indeed found in MMS observations [11,26], leading credence to the expectation that reconnection operates in a laminar manner at least some of the times and that 2.5D simulations are appropriate to model magnetopause reconnection. These models showed mixing of the two different source populations in the electron-scale vicinity of the reconnection X point

[24,25]. This paper shows that population mixing of electrons leads to complex, multi-component/structured distribution functions even in the larger ion-scale region.

A long-standing fundamental question in collisionless reconnection concerns how entropy is generated. Past MHD and PIC simulation studies have shown that entropy is conserved during reconnection except for the dissipation region (reconnection layer) [28]. An analytical calculation for pair-plasma reconnection [29] showed that entropy increases from the inflow to the outflow, indicating that irreversibility is introduced in the reconnection layer that processes the inflowing plasma to generate outflow exhausts. What happens in the reconnection layer and outflow to increase entropy in fully kinetic plasmas remains unanswered. Here we illustrate for guide-field asymmetric reconnection how structured distribution functions are formed in the magnetospheric separatrix region and exhaust, due to the mixing of otherwise disjoint magnetosheath and magnetospheric plasmas. Our results provide hints to how irreversibility may occur as reconnection opens gateways for the populations to mix. In addition, our study sheds light on the role acceleration mechanisms and magnetic topology changes play in establishing the reconnection jets, serving also as guidance for the interpretation of future spacecraft data.

II. MODEL AND RESULTS

Results presented here are from a high-resolution, particle-in-cell, simulation of magnetic reconnection in asymmetric configurations with a guide magnetic field of approximately unity. Details of the setup and model are discussed in recent work [25]. The initial magnetic field is given by $B_x = \left[0.5 + \tanh\left(z/l\right)\right]\cos\alpha + \sin\alpha$ and $B_y = -\left[0.5 + \tanh\left(z/l\right)\right]\sin\alpha + \cos\alpha$ with α=-14.87, l=0.5, and an initial X-type perturbation of amplitude 0.1 (the perturbation form and amplitude are inconsequential for the nonlinear phase of reconnection studied here). A mass ratio of m_i/m_e=25 is employed, and the ratio between plasma and electron cyclotron frequency is two. The electron-ion temperature ratio is T_e/T_i=0.2, and the initially uniform total temperature is $T=T_i+T_e$=1.5. The ratio between electron thermal velocity and the speed of light is approximately 0.2. The dimensions of the simulation domain are L_x=64 and L_z=25.6 ion inertial lengths (d_i) resolved by 1000 and 800 cells, respectively, with 6.4e9 particles. The simulation is designed to provide optimal signal-to-noise ratios for particle distributions (simulations with larger mass ratios and system size produce qualitatively similar results), following successes predicting observed distributions [11,24].

Figure (1) displays an overview of a subdomain of the simulated system around the in-plane null for the time of the peak reconnection rate, which is reached at approximately t=25 [20]. This rate varies slowly, it is within 10% of its peak value for about 16 ion cyclotron times [20]. Shown from top to bottom are the parallel electric field ($E_{||}$), the z-component of the electric field (E_z), the out-of-plane magnetic field (B_y), and the out-of-plane electron current density (j_{ye}), with in-plane magnetic field (white contours), and electron flow vectors (gold arrows whose lengths represent the flow magnitudes). The upper half plane represents the magnetosphere, and the lower models the magnetosheath.

The parallel electric field is positive in a d_i-scale region around the X point, a feature of guide field reconnection due to the projection of the reconnection electric field onto the guide magnetic field. The positive $E_{||}$ extends to the upper right. Electron outflows are strongly asymmetric, matching the gradients of the guide magnetic field, with strongly focused jetting to the right. To accommodate that motion through $\mathbf{E}_z\mathbf{x}\mathbf{B}_y$, the normal electric field E_z is strongly enhanced in a slab around the right separatrix. Note that E_z is positive in the left exhaust, while negative in the

right exhaust. The out-of-plane current density ($j_y \sim j_{ye}$, as the current is carried mainly by electrons) also shows substantial asymmetries, with a weaker, bifurcated, structure on the right and a single, much stronger, leg on the left.

Two types of population mixing will be elucidated in this paper. The first one corresponds to a type of nongyrotropic velocity distribution function (VDF) occurring in the region where E_z is highly enhanced. An example VDF obtained from the magnetospheric separatrix region at approximately 1 d_i from the X point and collected over an interval $\delta x=0.2$ and $\delta z=0.05$ d_i (a small fraction of the particle's Larmor radius) is shown in figure (2). The reduced distributions $f(v_x,v_y)$ and $f(v_x,v_z)$ exhibit two distinct components, where v_i is the particle velocity component in unit of the upstream magnetosheath Alfven velocity.

The mixing of particle populations suggested by the reduced VDFs is verified by means of tracing particles in the evolving electromagnetic fields backwards in time from the location of the distribution. Four typical particle orbits are shown (color coded with their respective source locations in the velocity space marked in figure 2 (top left two panels)), together with the contribution to particle energization by parallel and perpendicular electric fields (denoted as $\delta W_{\parallel}$ and $\delta W_{\perp}$, the integrated kinetic energy parallel and perpendicular to the magnetic field along the trajectory from an arbitrary point, respectively) for each. These particles originate either on the magnetosheath or the magnetosphere (red and green trajectories) side. For particles with orbits crossing regions of enhanced parallel electric field, primary acceleration is by the parallel electric field (green trajectory). The combination of magnetosphere particles with different degrees of parallel electric field acceleration leads to the field-aligned, cylindrical shape of the main part of the distribution function. This component is shifted toward $v_y<0$ as seen in the distribution $f(v_x,v_y)$ (top right panel), reflecting the acceleration ($v_y \sim v_{\parallel}$ at this location) by the positive $E_{\parallel}$ in the region encompassing the X point.

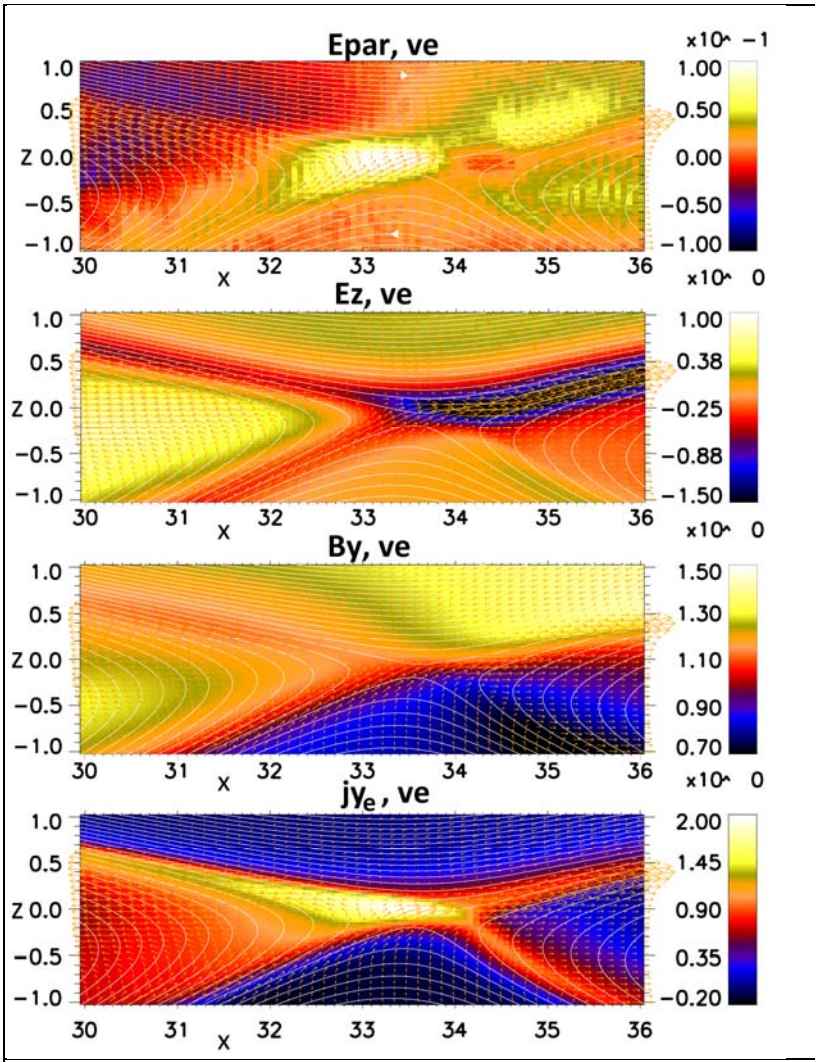

Figure 1. Structure of the d_i-scale region surrounding the in-plane X point at the time of the peak reconnection rate in asymmetric guide-field reconnection. From top to bottom, the parallel electric field, the z-component of the electric field, the out-of-plane magnetic field, and the out-of-plane electron current density. In each panel, the in-plane magnetic field is represented by the magnetic flux contours (white), and the in-plane electron flow velocity by arrows (gold). Length scales are normalized to the ion inertial length. The d_i-scale positive $E_{||}$ and the highly asymmetric E_z along the magnetosphere separatrices are outstanding features of guide-field asymmetric reconnection, and they are key to supporting the in-plane electron flow in the positive B_x region.

The second element is a strong enhancement of phase space density off the axis of the main component of $f(v_x,v_y)$, involving particles originating from the magnetosheath side (black and blue trajectories). These particles enter the right-side reconnection exhaust, and with finite Larmor radii, cross into the region of enhanced normal electric field E_z around the magnetosphere-side separatrix. During the upward part of their (distorted) Larmor orbit, these electrons experience acceleration by the strong perpendicular electric field, and deceleration on the downward leg. This phenomenon generates strong gyrophase dependence. At the energy peak, this acceleration has moved particles away from the thermal range, which combined with sampling only the upper part of the orbit (finite Larmor radius effect) leads to a crescent-type structure in $f(v_x,v_z)$. The larger phase space densities of the magnetosheath plasma make this the strongest component in the distribution. This accelerated magnetosheath population contributes to the fast electron outflow in the region of enhanced E_z. To date, nongyrotropic electron distribution functions of the type discussed in Figure 2 have been observed by the MMS mission in guide-field magnetopause reconnection [33] (see distribution 4 in Figure 6 of the paper). These observations provide confidence in the robustness of the simulation predictions.

The second type of population mixing occurs in the outflow region. As an example, a set of distributions is shown in figure 3 for a single flux tube in the left outflow region. We find the apparent combination of two different populations by a patching process, where one source population covers one range of parallel velocities, and the other source population covers the rest, directly abutting the former. Close inspection of figure 3 reveals that the location in velocity space where the two populations abut each other, as well as their relative contribution, appear to depend on the position along the field line. Specifically, a stronger contribution of the magnetosheath population is seen at the lower leg of the field line (B_x<0) whereas the magnetospheric population dominates in the upper leg (B_x>0), and stronger domination of the sheath (sphere) component further along the sheath (sphere) field line away from the B_x reversal.

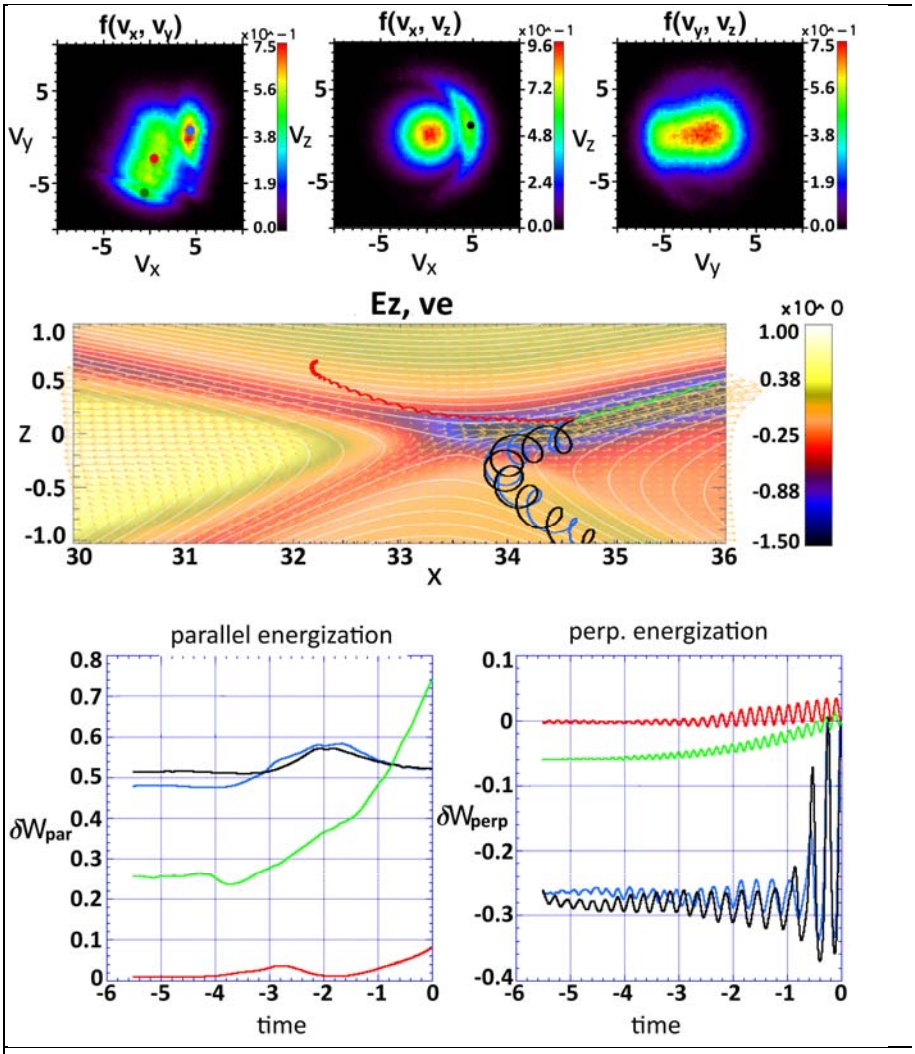

Figure 2. Crescent-type nongyrotropic distribution on magnetospheric field lines due to mixing of local inflow population with the magnetosheath electrons accelerated by E_z. The three reduced electron distributions at x=34.62 and z=0.12 (top panels), the traces of four particles contributing to the above distributions plotted on top of the poloidal magnetic field and the z component of the electric field, and the contributions of the parallel electric field (lower left) and the perpendicular electric field (lower right) toward overall particle energization. Final particle velocities are marked by the corresponding colors in the top left and center panels (same color codes as the orbits and energy changes).

The transition velocity between the two populations also depends on the position along the field line. This transition appears to be, at least in part, determined by a time-of-flight effect due to the ballistic motion of particles along the magnetic field after magnetic reconnection has occurred. Conceptually, this idea involves a magnetic disconnection and reconnection of a flux tube at t=0, which generates a segment containing magnetosheath particles patched together with a segment containing magnetospheric

particles. As time evolves, particles will follow their thermal motion along the magnetic field and create interpenetration of magnetospheric and magnetosheath populations. The transition occurs at the parallel velocity determined by the location along the field line as well as the time after field line reconnection. The transition velocity is approximately $v_{||}=L/t$, where L is the (signed) distance from the point of new connection along the field line, and t is the time since reconnection. Subsequent thermalization of the patched distributions and those shown in figure (2) will lead to entropy increase, and thereby contribute to the overall dissipative nature of the reconnection process.

The distributions near the magnetospheric separatrix exhibit a nongyrotropic feature, which merits further investigation. Particularly on the upper leg of the field line, closer to the magnetospheric side, the sheath component of the combined distribution exhibits asymmetry about the velocity direction parallel to B, whereas the magnetospheric part appears to be aligned well with the local magnetic field. Additional processes must be at work, beyond the relatively simple patching of populations.

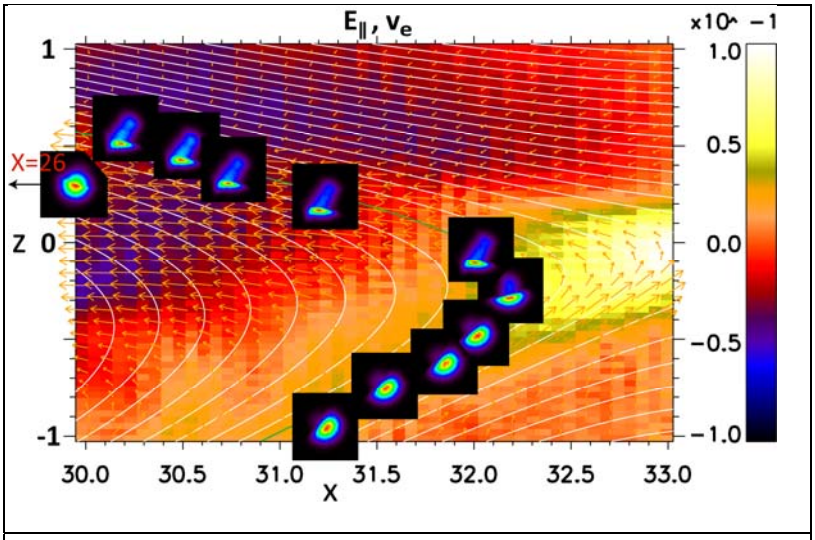

Figure 3. Set of reduced distributions $f(v_x,v_y)$ along a flux tube (center line colored green) shortly after it has been reconnected. The individual panels show the dependence of the structure on the location on the reconnected field line. The patched distributions combine the magnetosheath and magnetosphere inflow populations, and illustrate the result of breaking and rejoining of magnetic flux tubes during reconnection. The high phase-space-density magnetosheath population is an important contributor to the electron outflow in the region above the B_x reversal. The distribution to the far left, taken around x=26.11 and z=0.32, shows that distributions further downstream are increasingly isotropic.

In order to understand the processes responsible for this asymmetry, we investigate the distribution on the upper left of figure 3. All three reduced distributions are shown in the top panels of figure 4. We again trace particles backwards in time. The locations in velocity space from which particles are traced are indicated in the upper left panel of figure 4, together with the projection of the local magnetic field direction onto the v_x-v_y plane (red arrow). Five particles are integrated, two of which (green and black) originate from the magnetospheric side, and the other three (orange, red, and blue) from the magnetosheath side, as demonstrated by the orbits shown in figure 4.

All magnetosheath particles encounter enhanced parallel electric field, indicated by the bright yellow colors in the $E_{||}$ (center) panel. This parallel electric field changes particle energies appreciably (lower left panel of figure 4). The orange particle is energized the most, and the blue particle the least.

After acceleration, the magnetosheath particles travel down the magnetic field to the location where we calculate the distribution function. The bottom right panel of figure 4 shows that the gyrocenters of the three particles lie on progressively lower flux tubes, indicated by the dashed lines, which have been added to the orbit projections onto the x-z plane. The blue particle exhibits the smallest parallel velocity and the largest pitch angle, with a gyrocenter on a flux tube inward from our VDF location. This flux tube reconnected earlier than the one that contains the distribution function location. Consequently, a magnetosheath particle,with smaller parallel velocity had more time to propagate along the magnetic field to our location of interest compared to particles with gyrocenters located on more recently reconnected flux tubes. This is why the red particle has larger parallel velocity and smaller pitch angle, and,the orange particle has the largest $v_{||}$, but the smallest pitch angle. All particles contribute to the distribution function, which leads to the tilted magnetosheath feature in the top left panel. This new, dispersive, structure is the combined result of time-of-flight effects, parallel electric field acceleration, and finite Larmor radius effects.

Farther away from the upper separatrix and deeper inside the reconnected flux region, the increasing distance from the accessible boundary of magnetosheath electrons reduces asymmetries due to the finite Larmor radius effects. Consequently, distributions there (one example from further downstream is shown at the far left of figure 3) feature magnetosheath contributions more symmetric about the velocity direction parallel to the magnetic field. We expect again that the multi-component structures due to patching will eventually get smeared out (such as the distribution from x=26), e.g., by anisotropy-driven instabilities, and thus contribute to the overall entropy generation in collisionless magnetic reconnection.

III. DISCUSSION AND CONCLUSIONS

We used particle-in-cell simulations to demonstrate that multi-component electron distributions prevail not only in the X-point vicinity but also in the exhaust and separatrix regions of asymmetric magnetic reconnection with a significant guide magnetic field. We showed that population mixing occurs on magnetospheric (not yet reconnected) field lines due to finite Larmor radius effects of accelerated magnetosheath particles as well as on reconnected magnetic fields. Common on reconnected field lines is population patching - the simple result of ballistic propagation of magnetosheath and magnetospheric populations brought into contact by the reconnection process. A gyrotropic version of population patching has been observed [31,32], and recent observations also demonstrate nongyrotropic patching [33]. The patched distributions demonstrate the remarkable way reconnection mixes particles of different origins and different histories of acceleration by parallel and perpendicular electric fields. This mixing occurs even at significant distances from the X-point vicinity where structured distributions due to mixing are expected in principle [25,30]. Secondary instabilities and further mixing effects will likely conspire to reduce or eliminate these structures after longer time spans, leading to more isotropy. Similar effects should be expected for the ions as well, on their much larger scale lengths.

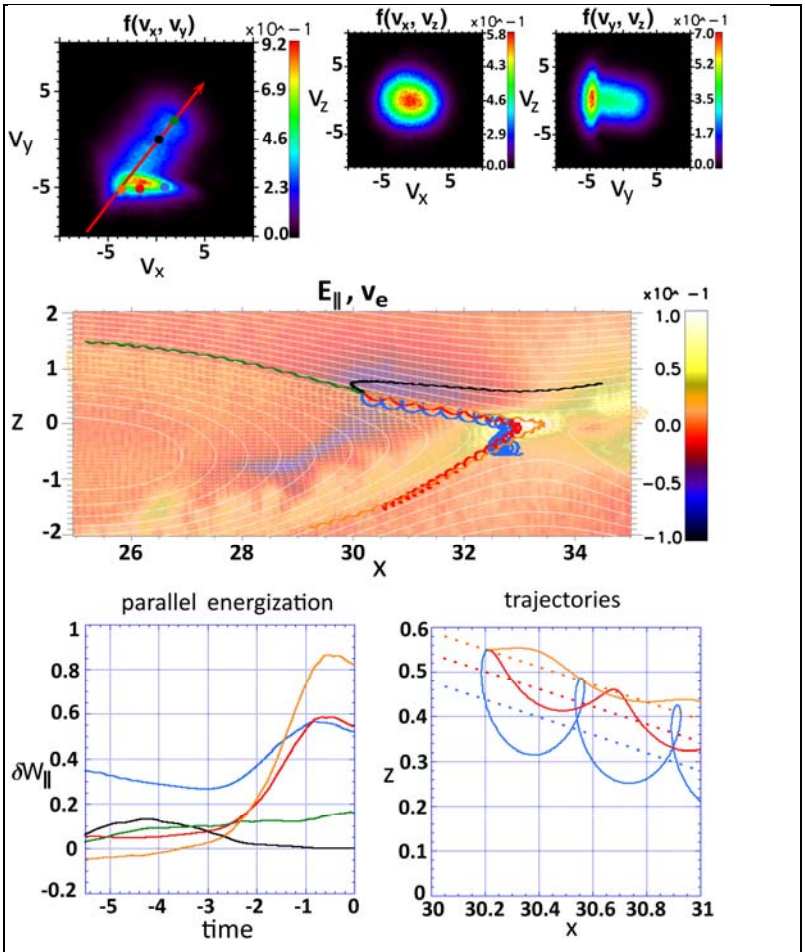

Figure 4. Three reduced electron distributions at x=30.21 and z=0.55 exhibiting a second type of nongyrotropy. The left panel, depicting $f(v_x,v_y)$, also shows the local projection of the magnetic field, as well as the phase space locations of five particles, which are traced backwards in time. All particle trajectories are plotted on top of the parallel electric field and the poloidal magnetic field in the middle panel. The bottom left panel depicts the energization due to $E_{||}$ for each of these particles – only magnetosheath particles are accelerated. The motion of the three sheath particles near the collection point is plotted together with the magnetic flux tubes coinciding with their gyrocenter locations.

In the region where the normal electric field is highly enhanced, the electron outflow is the fastest and is supported by $\mathbf{E}_z\mathbf{x}\mathbf{B}_y$ and the nongyrotropic magnetosheath component. In the left exhaust where the electron outflow is weaker and less focused than in the peak E_z region, parallel electric field acceleration combined with time-of-flight and finite Larmor radius effects shape the electron distributions, causing nongyrotropy and velocity dispersion near the magnetospheric separatrix. The parallel electric field in the d_i-scale region encompassing the in-plane X point is specific to guide-field reconnection and in part responsible for the asymmetries between the two exhausts, as it accelerates the magnetosheath electrons in the left exhaust, but decelerates sheath electrons in the right exhaust.

These results constitute predictions for the kinetic structures of guide-field asymmetric reconnection, and open up new grounds for future research with space missions such as MMS.

ACKNOWLEDGEMENTS

This work was funded by the NASA MMS project, and in part by grants from NASA-NNX16AG75G, DOE DESC0016278 and NSF AGS1619584, AGS-1202537, AGS-1543598, and AGS-1552142. Work at the University of Bergen was supported by the Research Council of Norway/CoE under contract 223252/F50. The authors recognize the tremendous effort in developing and operating the MMS spacecraft and instruments and sincerely thank all involved.

REFERENCES

[1] M. Yamada, et al., *Nature Communications*, 5: 4774 (2014).
[2] S. Masuda, T. Kosugi, H. Hara, S. Tsuneta, Y. Ogawara, *Nature*, **371**, 495-497 (1994).
[3] J. T. Gosling, R. M. Skoug, D. J. McComas, and C. W. Smith, *J. Geophys. Res*., **110**, A01107 (2005)
[4] P. Louarn, et al., *Space Sci. Rev., 187, 181-227 (2015).*
[5] G. Paschmann, *et al., Nature, 282, 243-246 (1979).*
[6] B. U. O□. Sonnerup, *et al*., *J. Geophys. Res*., **86**, 10049–10067 (1981).
[7] F. S. Mozer, S. D. Bale, and T. D. Phan, *Phys. Rev. Lett.*, **89**, 015002 (2002).
[8] P. A. Cassak and M. A. Shay, Phys. Plasmas **14**, 102114 (2007).
[9] J. L. Burch, T. E. Moore, R. B. Torbert, and B. L. Giles, *Space Sci. Rev*., **199**, 5-21 (2016).
[10] M. Hesse et al., *Space Sci Rev* **199**: 577. doi:10.1007/s11214-014-0078-y (2016)
[11] J. L. Burch, *et al.*, *Science*, doi:10.1126/science.aaf2939, (2016).
[12] M. Swisdak, B. N. Rogers, J. F. Drake, and M. A. Shay, *Journal of Geophysical Research*, **108,** doi:10.1029/2002JA009726 (2003).
[13] M. Swisdak, and J F Drake, *Geophysical Research Letters* **34** (11): L11106. doi:10.1029/2007GL029815 (2007).
[14] F. S. Mozer, P. L. Pritchett, J. Bonnell, D. Sundkvist, and M. T. Chang. *Journal of Geophysical Research* **113**: A00C03. doi:10.1029/2008JA013535 (2008).
[15] P. L. Pritchett and F. S. Mozer, *J. Geophys. Res.,* **114**, A11210 (2009).
[16] F. S. Mozer, and P. L. Pritchett, *Space Science Reviews* **158** (1): 119–43. doi:10.1007/s11214-010-9681-8 (2010).
[17] J. Egedal, A. Le, P. L. Pritchett, and W. Daughton, *Phys. Plasmas* **18**, 102901 (2011).
[18] S. Zenitani, M. Hesse, A. Klimas, and M. Kuznetsova, *Phys. Rev. Lett.* **106**, 195003 (2011).
[19] G. Paschmann, M. Øieroset, and T. Phan, *Space Sci. Rev.*, **178** (2–4), 385–417 (2013).
[20] M. Hesse, N. Aunai, S. Zenitani, M. Kuznetsova, and J. Birn, *Phys. Plasmas* **20** (6): 061210. doi:10.1063/1.4811467 (2013).
[21] Y-H. Liu, M. Hesse, and M. Kuznetsova, *J. Geophys. Res. Space Phys.*, **120**(9). DOI: 10.1002/2015JA021324 (2015).
[22] R. E. Ergun, *et al*., *Phys. Rev. Lett*., *116, 235102* (2016).
[23] S. Eriksson, *et al.,* P*hys. Res. Lett.*, **117**, 015001 (2016).
[24] M. Hesse, *et al*., *Geophys. Res. Lett.,* **41**, 8673–8680, doi:10.1002/2014GL061586 (2014). □
[25] M. Hesse, *et al*., *Geophys. Res. Lett.*, **43**, 069373 (2016).
[26] L.-J. Chen, et al., *Geophys. Res. Lett*., 43, 6036-6043 (2016).
[27] L.-J. Chen, M. Hesse, S. Wang, N. Bessho, and W. Daughton, *Geophys. Res. Lett*., **43**, 068243, (2016).
[28] J. Birn, M. Hesse, and K. Schindler, *Phys. Plasmas,* **13**, 092117 (2006).
[29] M. Hesse, S. Zenitani, M. Kuznetsova, and A. Klimas, *Phys. Plasmas* **16***,* 102106 (2009).
[30] M. Hesse, *Phys. Plasmas,* **13**, 122107, (2006).
[31] J. T. Gosling, *et al., Geophys. Res. Lett.,* **17**, 1833 (1990).
[32] M. Øieroset, *et al*, *J. Geophys. Res.,* **120**, 9294, doi:10.1002/2015JA021580 (2015).
[33] J. L. Burch, and T. D. Phan, *Geophys. Res. Lett.,* **43,** 8327–8338, doi:10.1002/2016GL069787 (2016). □